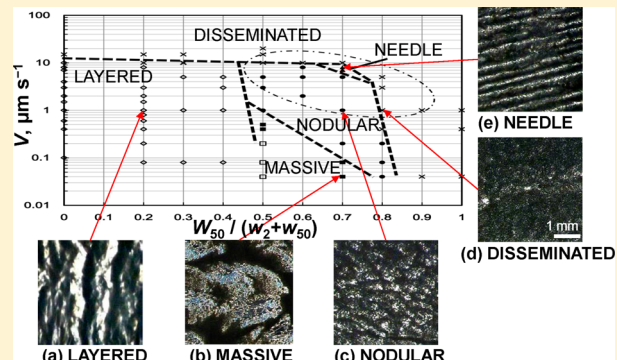


Growth Pattern Dependence of Tetrahydrofuran Hydrates in Glass Beads of Two Sizes on Growth Rate and Glass Bead Mixing Ratio

Michihiro Muraoka[#] and Kazushige Nagashima*

Department of Physics, School of Science and Technology, Meiji University, 1-1-1 Higashimita, Tama-ku, Kawasaki 214-8571, Japan

ABSTRACT: We observed the pattern formation of tetrahydrofuran (THF) clathrate hydrates in a mixture comprising a THF–17H₂O solution and glass beads of two sizes (2 and 50 μm diameter) as functions of growth rate and glass bead mixing ratios (by weight). The overall hydrate growth rate, V , was controlled using a directional growth apparatus. The results showed that the growth interface of the initial hydrate layer destabilized with growth. The wavelength, λ , of the destabilized initial hydrate layer demonstrated a power law decrease as the growth rate V increased. We successfully formed various hydrate patterns and classified them into a pattern diagram according to the glass bead mixing ratio and the growth rate V . In addition, we are the first to successfully obtain a needle pattern. Image analysis showed that the segregated growth area of the hydrates and the average hydrate area increased, whereas the number density of hydrate grains decreased with decreasing V . These results are qualitatively consistent with the frost heave model. Finally, we proposed needle, nodular, and massive pattern hydrate formation models by summarizing the discussions from the frost heave model and the morphological instability model of crystal growth.



1. INTRODUCTION

Clathrate hydrates are crystalline solid compounds consisting of a network of hydrogen-bonded water molecules and containing guest molecules enclosed in cavities. Large quantities of methane hydrates have been identified in sediment under the ocean floors. Knowledge of mechanisms concerning gas hydrate formation in ocean sediment are important for global climate change and energy resources issues.^{1,2}

Sediment cores recovered from ocean floors have been reported to contain various patterns (textures) and sizes of hydrates. These hydrates have been classified into four categories by Malone:³ disseminated (fine hydrates in the pore space of sediments), nodular (hydrates up to 5 cm in diameter), layered (parallel hydrate layers), and massive (as thick as 3–4 m, containing 95% hydrates and less than 5% sediment), as shown in Figure 7.8 of ref 1.

Malone proposed a simple model for hydrate formation in deep-sea sediments. In this model, the initially formed disseminated hydrate crystals grow to nodules, then to layers, and finally to a massive hydrate.³

Paull et al.⁴ provided a model for hydrate formation from free and recycled gases. In this model, the base of the gas hydrate stability (BGHS) field moves upward with progressive subsidence with time. Subsequently, the BGHS is displaced upward, leading to decomposing hydrates. Moreover, as hydrates decompose, the methane solubility limit is surpassed; thus, the so-called recycled rising gas bubbles permeate fissures in the overlying hydrate stability layer. Finally, a higher gas stability zone and layer are achieved.

Tohidi et al.⁵ and Katsuki et al.^{6,7} conducted visual observational studies of pore-scale hydrate formation and dissociation process on an etched glass plate to simulate the effect of porous media. These studies used a fixed sediment model on a glass plate for focusing on the disseminated type of hydrate. On the other hand, the freezing of water in soil is known to cause frost heave. In this phenomenon, growing ice crystals displace the soil particles and form a pure ice layer called an ice lens.^{8–10} In addition, this phenomenon is also reported growing He crystals¹¹ and Ar crystals¹² in porous media.

Most gas hydrates probably form from the aqueous phase in marine settings;¹³ however, the formation experiment of gas hydrate from aqueous phase has difficulty. The experiment and theoretical studies¹⁴ suggest that hydrate formation from dissolved gases in water might require an unrealistically long experimental time because the concentration of dissolved gas (CH₄, CO₂) in water is much lower than the concentration of gas in the hydrate at typical oceanic conditions.

Krause¹⁵ studied the origin of the zebra structure observed in brecciated blocks and clasts of the Meiklejohn Peak lime mud-mound (Bare Mountain Quadrangle, NV, USA) formed in the Early Middle Ordovician. The interior of the mound is typified by light gray limestone with zebra band structures (similar to a layered pattern). Comparing observed images and the zebra structure, layered pattern methane hydrate, and segregated ice

Received: February 28, 2014

Revised: June 3, 2014

Published: June 19, 2014



lenses observed in soil (frost heave), Krause postulated that the zebra structure in the Meiklejohn Peak lime mud-mound formed accompanied by the formation of layered pattern CO₂ gas hydrate.

Clennell et al.¹⁶ proposed a conceptual model for hydrate formation in sediment based on a formation model of ice in freezing soil.¹⁷ This model predicts that the inner pressure (phase pressure) of the hydrates, which is elevated by the capillary effect in fine-grained sediment, exceeds the effective confining stress combined with the tensile strength of the sediment, and the hydrates displace the sediment to form hydrate patterns.

Although some models and experimental studies of gas hydrate formation in sediment models and in soil have been performed, the formation mechanism of hydrate patterns such as the layered, nodular, and massive types is not yet understood. Experimental studies of gas hydrate tend to form the disseminated type of hydrates. The tetrahydrofuran (THF)-water system is useful as an idealized experimental hydrate model system. THF is miscible with water at all molar ratios, and a stoichiometric THF-water solution (THF-17H₂O) forms a structure-II hydrate¹⁸ below 4.4 °C at atmospheric pressure.¹⁹

Our group^{20–22} performed growth experiments of THF hydrates in a mixture of glass beads and the stoichiometric THF-water solution using a directional growth technique.^{23,24} We believe that this model system has the advantage to use in a step-by-step approach. As a first step, only the effect of the sediment was studied by using stoichiometric THF-water solution to eliminate the diffusion-limited effect of guest molecules. Note that both sediment effect and diffusion-limited effect of guest molecules can be studied using dilute THF-water solution as a second step.

Suzuki et al.²⁰ studied isolated silica particle behavior at the growth interface of THF hydrates in a THF-water solution. The results showed that the growth interface displaced the beads at lower growth rates than a critical growth rate V_c which was nearly inversely proportional to the bead diameter. This trend corresponds to the theoretical result for the foreign particle behavior of a growing ice crystal.²⁵ The theory assumes that the particle is displaced by the repulsive interaction deriving from the difference in interfacial energies between a particle, liquid, and ice. In addition, when the particle is being displaced in the liquid, an opposing force will arise from viscous drag. By balancing the two forces, the critical growth rate is derived to be inversely proportional to the particle diameter.

Nagashima et al.²¹ showed that the layered pattern formed when 2-μm-glass beads were used, and the disseminated pattern formed when 50-μm-glass beads were used. On the other hand, Muraoka et al.²² showed that the nodular and massive patterns formed when the two bead sizes were mixed. On the basis of these results, we considered that it is important to clarify how the patterns change from layered to nodular, massive, and disseminated depending on the mixing ratio of the glass beads.

In this study, we investigated pattern formation of hydrates in a mixture comprising 2- and 50-μm-glass beads and a THF-17H₂O solution using a directional growth apparatus based on the apparatus used in our previous studies.^{20–22} The objective was to clarify the effects of not only the growth rate but also the weight ratio of the 2- and 50-μm beads on pattern formation. The formed hydrate patterns were classified into a diagram in accordance with the growth rate and the glass bead mixing ratios. The obtained images of the various hydrate patterns

were analyzed, and the results are discussed in relationship to the frost heave model.

2. EXPERIMENTAL SECTION

2.1. Materials. The reagents, THF-water solution composition, and the glass beads used in the sediment model were the same as those used in our previous studies.^{21,22} Sediment model system samples comprised a mixture of spherical glass beads and a THF-water solution (THF-17H₂O). Dehydrated stabilizer-free THF (99.5 wt % purity, Kanto Chemical Inc.) and ultrapure water (18.2 MΩ cm resistivity) were used as the reagents. The mean glass bead diameters were 2 μm (silica microbeads P-600, Catalysts and Chemicals Ind. Co. Ltd.) and 50 μm (Unibead SPL-50, Union Co Ltd.), and both types of beads were composed of pure silica. The two sizes of beads were mixed at a weight ratio, $w_2:w_{50}$, where w_2 is the weight of the 2-μm beads and w_{50} is the weight of the 50-μm beads. The $w_2:w_{50}$ ratio was variable in this study. In our previous studies, the $w_2:w_{50}$ ratios used were 10:0, 0:10,²¹ and 5:5.²² The gravimetric solution content in the sample was defined as w_s/w_g , where w_s is the weight of the THF-water solution and w_g is the weight of the glass beads. The w_s/w_g value in this study, [$w_s/(w_2 + w_{50})$], was 1.0, which is the same as that employed in the studies by Nagashima et al.²¹ and Muraoka et al.²²

2.2. Experimental Methods. In this study, the same experimental system and methods as those shown in ref 22 were used and are briefly described as follows. The growth cell comprises two glass plates (25 mm × 150 mm × 1 mm) and spacers (0.5 mm thick) that are inserted between them. The growth cell was set in a directional growth apparatus which consists of a cold block (lower than the equilibrium temperature, T_{eq}) and hot block (higher than T_{eq}). Then, the temperature gradient G (= 1.3 K mm⁻¹) was applied to the growth cell. Hydrate crystals were compulsorily nucleated using a chilled wire at the edge of the growth cell in the colder region. A pure hydrate layer was initially formed by maintaining a stationary condition of the growth cell for 20 min after nucleation. The growth cell was then moved at a constant velocity ($\geq 0.04 \mu\text{m s}^{-1}$) toward the cold block. The overall hydrate growth rate, V , could be controlled by controlling the velocity of the growth cell. The movement distance of the growth cell (i.e., the total length of the hydrate growth region) was 25 mm. The patterns of the hydrates formed were observed using a digital microscope (VH-S500, KEYENCE Co. Ltd.), and images of the hydrates were recorded as digital image files on a personal computer.

To evaluate size scales of hydrate grains and the number density, the obtained images of nodular type, massive type, and disseminated type hydrates were processed by Method II (an image processing method retaining the relatively large hydrate regions) proposed by Muraoka et al.²² The very small white dots caused by electrically induced noise and by light transmitted through the 50-μm beads were removed prior to image processing by Method II. The threshold value for white dot removal was 2500 μm² (50 × 50 μm). Images were processed and analyzed using the image processing program ImageJ 1.44p (National Institutes of Health, USA).

3. RESULTS

3.1. Morphological Instability of the Growth Interface in the First Stage. Figure 1 shows sequential images of the formation of the initial hydrate layer formed in the sediment model for $w_2:w_{50} = 8:2$ and $V = 0.2 \mu\text{m s}^{-1}$. The white regions of the images indicate the hydrates formed by displacing the glass beads, whereas the black and dark gray regions indicate glass bead-rich regions where hydrates formed in the pore space of the sediment model. The hydrate growth direction is toward the right of the images, which applies to all images in this report.

Figure 1a shows the initial hydrate layer formed at $t = 0$ s (after 20 min from compulsory nucleation). After the compulsory nucleation of hydrates, THF hydrate formed in the region colder than the melting point. Consequently, the

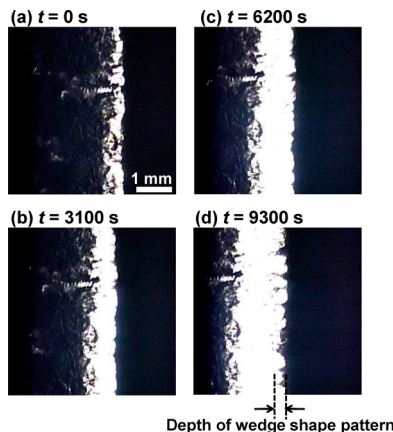


Figure 1. (a–d) Sequential images of the formation process of the initial hydrate layer formed in the sediment model for $w_2:w_{50} = 8:2$ and $V = 0.2 \mu\text{m s}^{-1}$. The same scale bar applies to all the images.

initial hydrate layer formed by displacing the glass beads along the isothermal line. Figure 1b shows an image of the growth interface at $t = 3100$ s. The hydrate layer has become wider than that at $t = 0$ s because the growing hydrate layer has displaced the glass beads. In addition, the growth interface of the hydrate has gradually destabilized, and a wedge-shaped pattern has formed at the interface. At $t = 6200$ s (Figure 1c), the hydrate layer has become wider. The depth of the wedge shape pattern has also become larger. At $t = 9300$ s (Figure 1d), the depth of the wedge shape pattern has obtained a maximum, and the growth of the initial hydrate layer stopped. Subsequently, a new hydrate layer has begun to form to the right of the image (not shown).

Figure 2 shows images of the destabilized patterns of the initial hydrate layer when the widths of the initial hydrate layers

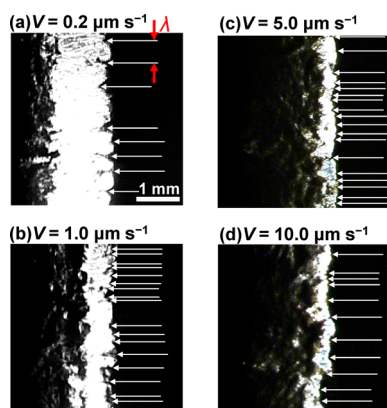


Figure 2. (a–d) Images of the destabilized pattern of the initial hydrate layer when the width of the initial hydrate layer is at a maximum for $V =$ (a) 0.2, (b) 1.0, (c) 5.0, and (d) $10.0 \mu\text{m s}^{-1}$. The white arrows indicate the concave points of the wedge-shaped growth interface. The red arrows indicate the interval λ of the neighboring concave bottoms of the wedge shapes. The same scale bar applies to all the images.

are maximum for $V =$ (a) 0.2, (b) 1.0, (c) 5.0, and (d) $10.0 \mu\text{m s}^{-1}$. The white arrows in the images indicate concave points of the wedge shapes. The red arrows in Figure 2a show intervals of the neighboring concave bottoms of the wedge shapes, and this interval is referred to as the wavelength, λ , in this report. The destabilized pattern formation process was observed at $V \leq 5 \mu\text{m s}^{-1}$.

However, the initial hydrate layer immediately stopped growing and began to encapsulate the glass beads after $t = 0$ s at $V = 10 \mu\text{m s}^{-1}$ (i.e., the destabilized pattern formation process was not observed). The results showed that λ decreased as V (for $V \leq 5 \mu\text{m s}^{-1}$) increased. Note that, at a higher V range ($V > 5 \mu\text{m s}^{-1}$), the destabilized pattern formation process might be incomplete because the initial hydrate layer immediately stopped growing.

Figure 3 shows the wavelength, λ plotted against V for various values of $w_2:w_{50}$. The values for λ were obtained by

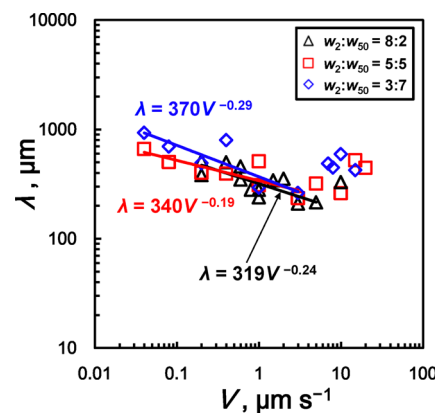


Figure 3. Relationship between λ and V for $w_2:w_{50} = 8:2$, 5:5, and 3:7.

averaging the measured values from the overall growth interfaces in the images. The wavelength, λ , decreased as V ($V \leq 5 \mu\text{m s}^{-1}$) increased for each $w_2:w_{50}$. The solid lines indicate the best linear fit to the data ($V \leq 5 \mu\text{m s}^{-1}$). The values of λ are characterized by power laws as a function of V , such as $\lambda = 319V^{-0.24}$ ($w_2:w_{50} = 8:2$), $\lambda = 340V^{-0.19}$ ($w_2:w_{50} = 5:5$), and $\lambda = 370V^{-0.29}$ ($w_2:w_{50} = 3:7$). In contrast, the wavelengths in the higher growth rate region ($V > 5 \mu\text{m s}^{-1}$) do not agree with the trend since the destabilized pattern formation process of the initial hydrate layer stopped immediately after $t = 0$, and λ was not influenced by V .

3.2. Hydrate Pattern Development of Initial–Middle–Final Stages. Figure 4 shows the entire images of hydrates formed in the sediment model under two types of experimental conditions. The white areas in the images show the hydrate regions, and the black and dark gray areas show the glass bead-

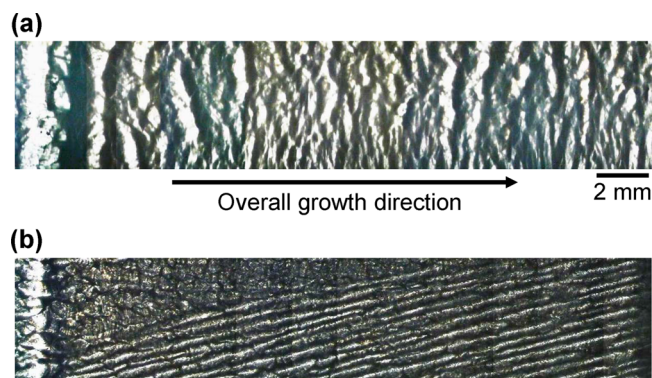


Figure 4. Entire images of hydrates formed in the sediment model for two types of experimental conditions: (a) $w_2:w_{50} = 8:2$ and $V = 1.0 \mu\text{m s}^{-1}$, and (b) $w_2:w_{50} = 3:7$ and $V = 8.0 \mu\text{m s}^{-1}$. The same scale bar applies to all the images.

rich regions. The vertical white lines on the leftmost sides of the images indicate the initially formed hydrate layer just after compulsory nucleation. The overall growth direction is toward the right of the images and is indicated by the arrow. Therefore, the rightmost sides of the images correspond to the region just before the end of the run.

Figure 4a shows the entire image of hydrates formed for $w_2:w_{50} = 8:2$ and $V = 1.0 \mu\text{m s}^{-1}$. The initial hydrate layer was formed at the leftmost side of the image as mentioned above. As growth proceeded, new layers were formed repeatedly until the end of the run, leading to the formation of multilayered patterns. The thickness of the hydrate layer and that of the intervals between neighboring hydrate layers gradually decreased from the initial stage to the middle stage. The thickness of the hydrate layer and that of intervals between layers were almost constant from the middle stage to the end of the run (final stage).

Figure 4b shows the entire image of hydrate formed for $w_2:w_{50} = 3:7$ and $V = 8.0 \mu\text{m s}^{-1}$. The vertical white line on the leftmost side of the image indicates the initially formed hydrate layer as mentioned. After the initial hydrate layer formed, the layered pattern changed to the nodular (upper side on the image) and needle patterns (lower side on the image). Subsequently, the region where needle pattern formed increased from the initial stage to the middle stage, and the sizes were nearly constant from the middle stage to the end of the run (final stage).

The entire image of hydrate formed at $w_2:w_{50} = 10:0$ is shown in Figure 2a of ref 21, and the entire image at $w_2:w_{50} = 5:5$ is shown in Figures 3 and 5 of ref 22. After the initial hydrate layer formed, various hydrate patterns developed depending on the mixing ratio of the glass beads, $w_2:w_{50}$, and the growth rate, V . For each experimental run, the hydrate patterns and sizes were almost constant from the middle to the end of the run (i.e., steady-state growth was observed). This trend agrees with the results of Nagashima et al.²¹ and Muraoka et al.²² Therefore, the hydrate patterns formed in the final stage were adopted for analysis.

3.2.1. Hydrate Patterns Formed at Various V for $w_2:w_{50} = 8:2$. Figure 5 shows the steady-state hydrate patterns formed in the final stage of different runs with different values of V for $w_2:w_{50} = 8:2$. The white areas in the images show the hydrate regions, and the black and dark gray areas show the glass bead-rich regions. The image obtained at $V = 10.0 \mu\text{m s}^{-1}$ (Figure 5a) is almost totally black. This corresponds to the

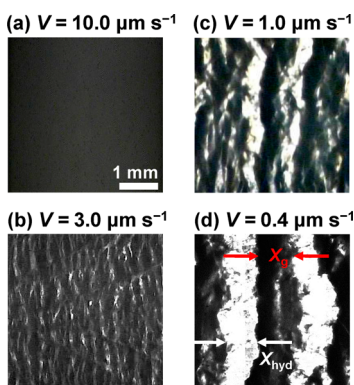


Figure 5. Steady-state hydrate patterns in the sediment model with V values ($\mu\text{m s}^{-1}$) of (a) 10.0, (b) 3.0, (c) 1.0, and (d) 0.4 for $w_2:w_{50} = 8:2$. The same scale bar applies to all the images.

disseminated pore space type. Figure 5 also shows the periodic hydrate layered pattern formed at $V = 3.0 \mu\text{m s}^{-1}$ (Figure 5b), $1.0 \mu\text{m s}^{-1}$ (Figure 5c), and $0.4 \mu\text{m s}^{-1}$ (Figure 5d). Both X_{hyd} (the average thickness of the hydrate layer) and X_g (the average thickness of the intervals between neighboring hydrate layers) increased as V decreased.

Figures 6, panels a and b show the relationships between X_{hyd} and V , and between X_g and V , respectively, along with those

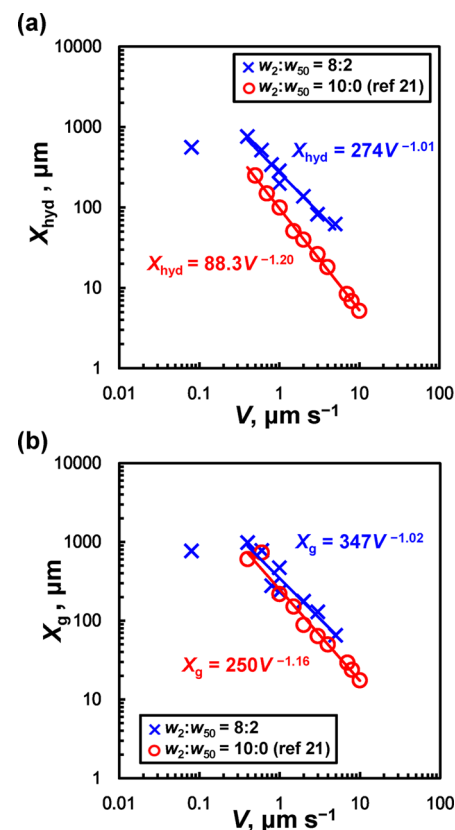


Figure 6. Relationships between (a) X_{hyd} and V , and (b) X_g and V for $w_2:w_{50} = 8:2$ and $w_2:w_{50} = 10:0$. The data points for $w_2:w_{50} = 10:0$ are adopted from the study of Nagashima et al.²¹ Note that the fitting lines were obtained while neglecting the outlier at $V = 0.08 \mu\text{m s}^{-1}$.

relationships determined in ref 21 (for $w_2:w_{50} = 10:0$) for comparison. The values for X_{hyd} and X_g were obtained by averaging 10 measured values. The results show that X_{hyd} and X_g can be characterized by power laws as a function of V , such as $X_{\text{hyd}} = 274V^{-1.01}$ and $X_g = 347V^{-1.02}$. Note that the fitting was conducted while neglecting the outlier at $V = 0.08 \mu\text{m s}^{-1}$. The results suggest that both size scales were inversely proportional to V . This trend of results nearly corresponds to the results of Nagashima et al.²¹ (for $w_2:w_{50} = 10:0$).

3.2.2. Hydrate Patterns Formed at Various Values of V for $w_2:w_{50} = 3:7$. Figure 7 shows the steady-state hydrate patterns in the final stage of different runs with different values of V for $w_2:w_{50} = 3:7$. Figure 7a shows that needle-like hydrates formed nearly in the direction of the overall growth (i.e., the x -axis direction) at $V = 8.0 \mu\text{m s}^{-1}$. The thickness of this hydrate, Y_{hyd} , in the y -axis direction is approximately 0.16 mm. This pattern does not correspond to any of the four types of hydrate patterns categorized by Malone.³ This steady-state hydrate pattern is referred to as the “needle” pattern in this report. This needle pattern was observed with high reproducibility under

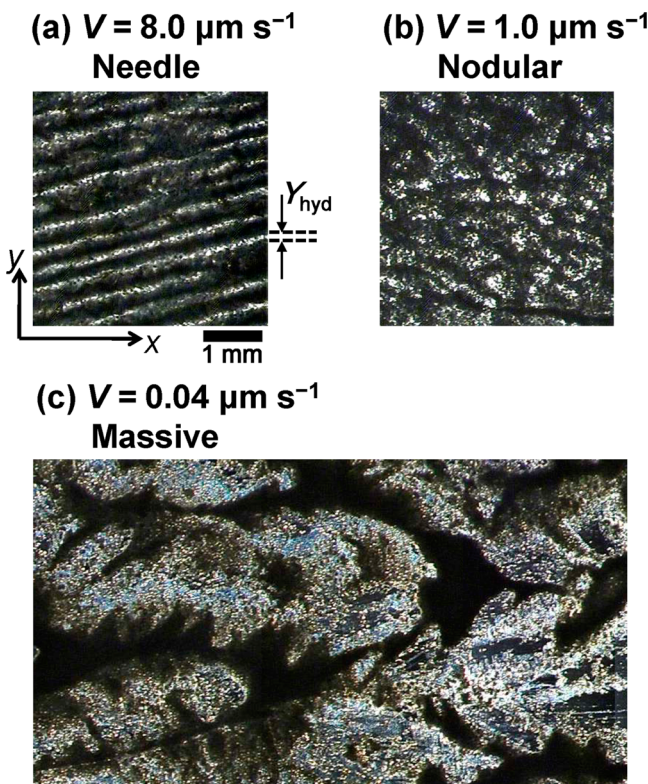


Figure 7. Steady-state hydrate patterns in the sediment model with V values ($\mu\text{m s}^{-1}$) of (a) 8.0, (b) 1.0, and (c) 0.04 for $w_2:w_{50} = 3:7$. The same scale bar applies to all the images.

experimental conditions nearby $w_2:w_{50} = 3:7$ and $V = 8.0 \mu\text{m s}^{-1}$. The disseminated type whose image looks almost black formed at V higher than $8.0 \mu\text{m s}^{-1}$ (not shown). However, the nodular type formed at $V = 1.0 \mu\text{m s}^{-1}$ (Figure 7b) and at V lower than $8.0 \mu\text{m s}^{-1}$. Figure 7c shows that the massive type hydrate formed at $V = 0.04 \mu\text{m s}^{-1}$. Finally, the needle pattern formation suggests that an undiscovered pattern of methane hydrate might exist under the ocean floor.

3.2.3. Hydrate Patterns Formed at Various Values of V for $w_2:w_{50} = 2:8, 0:10$. Figure 8 shows the steady-state hydrate patterns in the final stage of different experimental runs with different values of V for $w_2:w_{50} = 2:8$. There are two small hydrate grains in Figure 8a ($V = 1.0 \mu\text{m s}^{-1}$); however, the disseminated type is observed to have formed in the overall image. Similarly, the disseminated type formed at $V > 1 \mu\text{m s}^{-1}$ (not shown). The nodular type hydrate formed at $V = 0.2 \mu\text{m s}^{-1}$ (Figure 8b) and $V = 0.04 \mu\text{m s}^{-1}$ (Figure 8c). The size of hydrate grains increased as V decreased. At $w_2:w_{50} = 0:10$ (50- μm beads only), only the disseminated type formed even at the lowest growth rate of $0.04 \mu\text{m s}^{-1}$ (not shown).

3.2.4. Hydrate Pattern Dependence for Various $w_2:w_{50}$ Values at $V = 1.0 \mu\text{m s}^{-1}$. Figure 9 shows the steady-state hydrate patterns in the final stage of different runs for different values of $w_2:w_{50}$ at $V = 1.0 \mu\text{m s}^{-1}$. Each image is arrayed in the order of increasing mixing ratio of 50- μm beads: $w_2:w_{50} = 8:2$ (a), 6:4 (b), 5:5 (c), 3:7 (d), and 2:8 (e). Figure 9 indicates that the layered hydrate pattern (Figure 9a) changed to a collapsed layer (Figure 9b) and then to nodular (Figure 9c,d) and disseminated (Figure 9e) with increasing mixing ratio of 50- μm beads.

3.2.5. Diagram of Hydrate Patterns at Various Values of V and $w_2:w_{50}$. Figure 10 shows the diagram of hydrate patterns

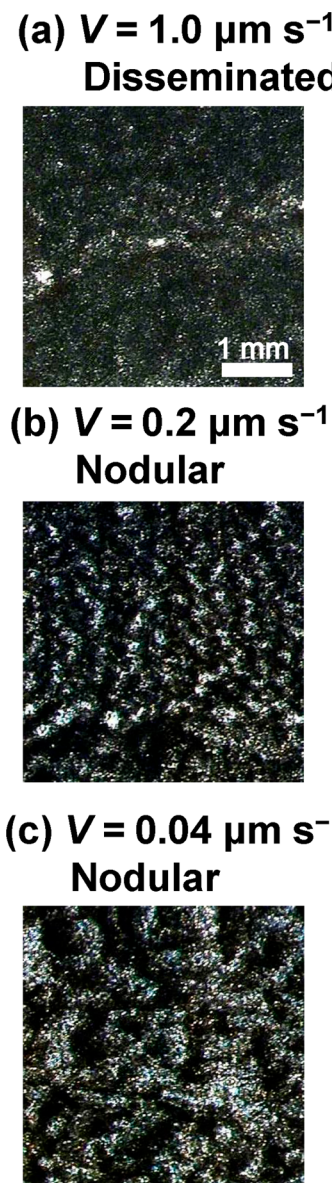


Figure 8. Steady-state hydrate patterns in the sediment model with V values ($\mu\text{m s}^{-1}$) of (a) 1.0, (b) 0.2, and (c) 0.04 for $w_2:w_{50} = 2:8$. The same scale bar applies to all the images.

(i.e., the dependence of hydrate patterns on V and $w_2:w_{50}$). The horizontal axis indicates the mixing ratio of 50- μm beads, $w_{50}/(w_2 + w_{50})$, wherein this value increases as the weight ratio of 50- μm beads increases. The data points in Figure 10 are indicative of steady-state hydrate patterns. The markers represent the layered (open diamond (\diamond))), nodular (filled circle (\bullet))), massive (filled square (\blacksquare))), needle (filled triangle (\blacktriangle))), and disseminated (diagonal cross (\times))) type hydrates. The data points at $w_{50}/(w_2 + w_{50}) = 0$ (i.e., 2- μm beads only) and in the range of $0.4 \mu\text{m s}^{-1} \leq V \leq 12 \mu\text{m s}^{-1}$ are adopted from the study of Nagashima et al.²¹ Similarly, the data points at $w_{50}/(w_2 + w_{50}) = 0.5$ (i.e., $w_2:w_{50} = 5:5$) are adopted from the study of Muraoka et al.²² Note that, at $V = 0.2 \mu\text{m s}^{-1}$ and $w_{50}/(w_2 + w_{50}) = 0.5$, the massive hydrate formed in the middle stage of the run; however, only the two layers of the hydrates formed in the final stage are as shown in Figure 5a in ref 22. Therefore, it was difficult to judge if the hydrate pattern reached a steady state. This growth condition might be the

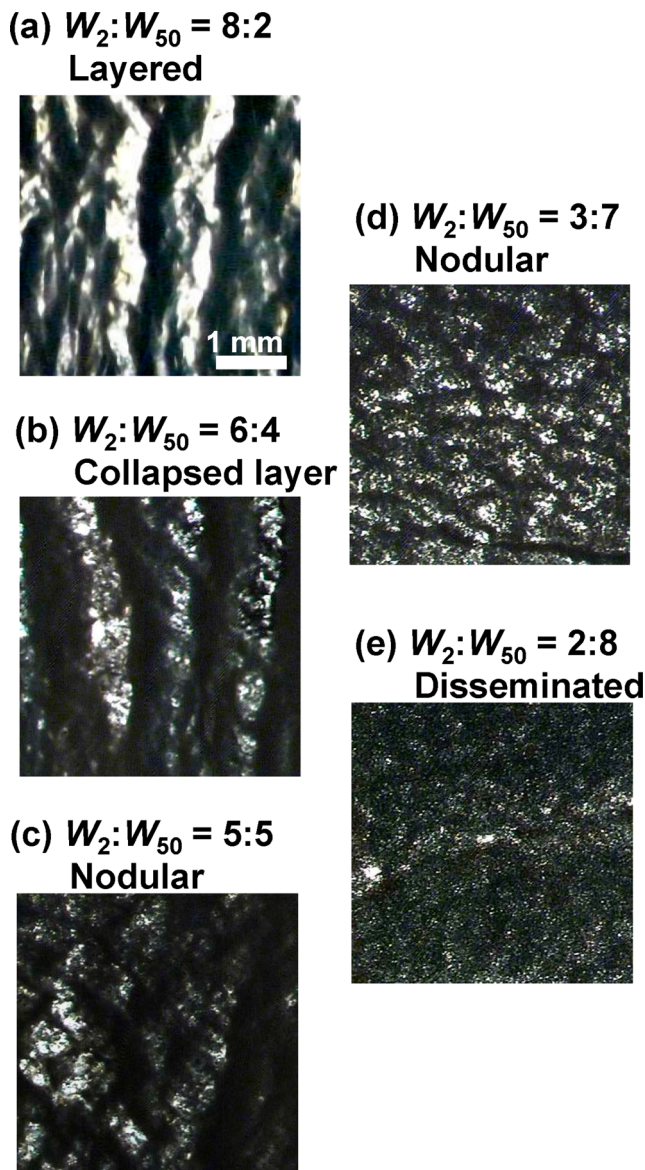


Figure 9. Steady-state hydrate patterns in the sediment model for $w_2:w_{50} =$ (a) 8:2, (b) 6:4, (c) 5:5, (d) 3:7, and (e) 2:8 at $V = 1.0 \mu\text{m s}^{-1}$. The same scale bar applies to all the images.

critical condition between the observance of massive and layered hydrates, and this exceptional case is shown by an open square (\square). Similarly, at $V = 0.08 \mu\text{m s}^{-1}$ and $w_{50}/(w_2 + w_{50}) = 0.5$, and at $V = 0.04 \mu\text{m s}^{-1}$ and $w_{50}/(w_2 + w_{50}) = 0.5$, as shown in Figure 5b,c in ref 22, the massive hydrate formed in the middle stage of the run; however, the size of the hydrate regions drastically diminished in the final stage. Therefore, it was difficult to judge whether the pattern had reached steady-state in this case as well. These exceptional patterns are shown by open squares (\square), as well. A break line indicates the boundary between each pattern.

The results indicate that, in the left region of the diagram (2- μm -bead-rich region), the layered type formed; however, the disseminated type formed in the higher V region. When the ratio of 50- μm beads is quite large (the rightmost region of the diagram), the disseminated type formed regardless of the value of V . When the ratio of 50- μm beads is medium and higher, the nodular type formed. However, the disseminated type formed with high V , and the massive type formed with low V . The

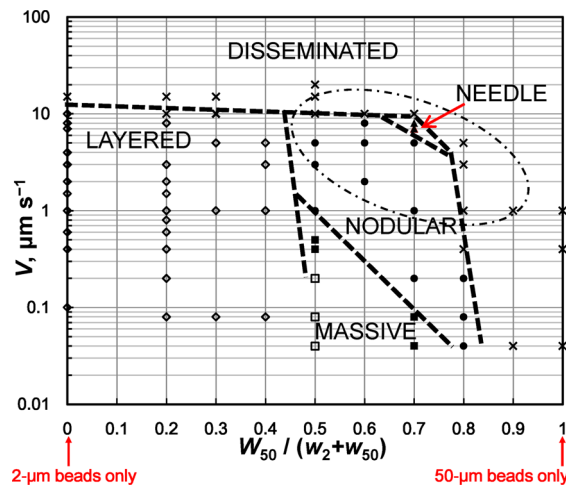


Figure 10. Diagram of hydrate patterns for various values of V and $w_{50}/(w_2 + w_{50})$. The markers represent the layered (open diamond (\diamond)), nodular (filled circle (\bullet)), massive (filled square (\blacksquare)), needle (filled triangle (\blacktriangle)), and disseminated types (diagonal cross (\times)), respectively. The open squares (\square) represent the critical pattern between the layered and massive patterns. The data points at $w_{50}/(w_2 + w_{50}) = 0$ (for 2- μm beads only) and in the V range of $0.4 \mu\text{m s}^{-1} \leq V \leq 12 \mu\text{m s}^{-1}$ are adopted from the study of Nagashima et al.²¹ Similarly, the data points at $w_{50}/(w_2 + w_{50}) = 0.5$ ($w_2:w_{50} = 5:5$) are adopted from the study by Muraoka et al.²²

needle pattern formed at $w_{50}/(w_2 + w_{50}) = 0.7$ (i.e., $w_2:w_{50} = 3:7$) and $V = 7.0\text{--}8.0 \mu\text{m s}^{-1}$. In addition, the needle pattern was observed partly under nodular and disseminated type formation conditions close to the needle formation condition, indicated by the dashed-dotted line in the figure. This region is referred to as the semineedle region in this report. Thus, the results of systematic experimental runs are summarized in a diagram of hydrate patterns as a function of V and $w_{50}/(w_2 + w_{50})$.

The boundaries between the disseminated and nodular, and the nodular and massive type were decided by not only the visual appearance but also by using the quantitative method proposed by Muraoka et al.²² The results will be shown in the following section.

3.3. Size Scale of Various Pattern Hydrates As a Function of V and $w_2:w_{50}$. The nodular and massive type hydrates formed at $w_2:w_{50} = 3:7$ and 2:8 were processed by Method II, as discussed in section 2.2. The total segregated hydrate area, S_{hyd} , the total area of the image used, S_{img} , and the total number of hydrate grains, N , were obtained. The data points for $w_2:w_{50} = 5:5$ (Figures 11–13) are adopted from Muraoka et al.²² for comparison.

Figure 11 shows the ratio of the total hydrate area to the area of the image used, $S_{\text{hyd}}/S_{\text{img}}$ plotted against V for $w_2:w_{50} = 5:5$, 3:7, and 2:8. The ratio $S_{\text{hyd}}/S_{\text{img}}$ was used to evaluate the segregated growth area of the hydrates. In the highest V range ($10 \mu\text{m s}^{-1} \leq V \leq 20 \mu\text{m s}^{-1}$) for $w_2:w_{50} = 5:5$, $S_{\text{hyd}}/S_{\text{img}}$ was 0 (does not appear in the graph) because all the quite small white dots in the original binary images were smaller than the noise reduction method threshold. We determined that $S_{\text{hyd}}/S_{\text{img}}$ could be classified into three (for $w_2:w_{50} = 5:5$, 3:7) or two (for $w_2:w_{50} = 2:8$) regions with different orders of magnitude. These regions are circled in Figure 11, and the types of hydrates observed are denoted under each circle. The regions surrounded by the solid line indicate the region where the massive or nodular type forms. The regions surrounded by the

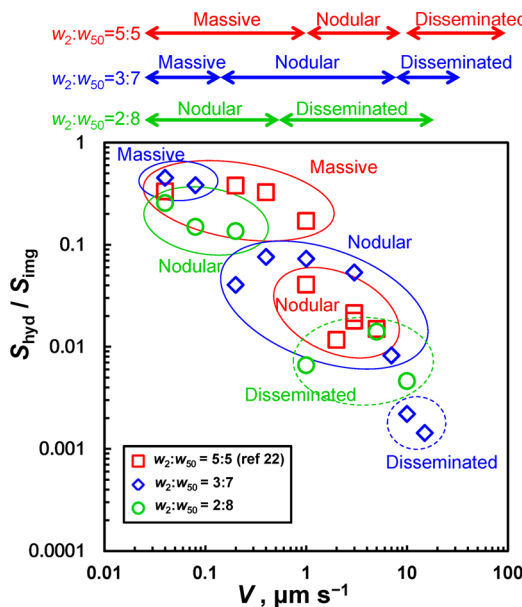


Figure 11. Relationship between $S_{\text{hyd}}/S_{\text{img}}$ (the ratio of the total hydrate area, S_{hyd} , to the total area of the image used, S_{img}) and V for $w_2:w_{50} = 5:5$, 3:7, and 2:8. The data points at $w_2:w_{50} = 5:5$ are adopted from Muraoka et al.²²

dashed line indicate the region where the disseminated type forms. The double-headed arrows indicate the V range for each type of hydrate formed.

$S_{\text{hyd}}/S_{\text{img}}$ decreased as V increased for all values of $w_2:w_{50}$. For $w_2:w_{50} = 3:7$ in the lowest V range ($0.04 \mu\text{m s}^{-1} \leq V \leq 0.08 \mu\text{m s}^{-1}$), $S_{\text{hyd}}/S_{\text{img}}$ was the largest, ranging from 0.4 to 0.5. $S_{\text{hyd}}/S_{\text{img}}$ discontinuously decreased at $V = 0.2 \mu\text{m s}^{-1}$. In the range of $0.2 \mu\text{m s}^{-1} \leq V \leq 7.0 \mu\text{m s}^{-1}$, $S_{\text{hyd}}/S_{\text{img}}$ ranged from 0.008 to 0.07, which is 1 or 2 orders of magnitude lower than those found in the lowest range of V . In the highest range of V ($10 \mu\text{m s}^{-1} \leq V \leq 15 \mu\text{m s}^{-1}$), $S_{\text{hyd}}/S_{\text{img}}$ was approximately 0.001. These three velocity range groups correspond to those classified by visual appearance: massive, nodular, and disseminated pore space types.

For $w_2:w_{50} = 2:8$ in the lowest V range ($0.04 \mu\text{m s}^{-1} \leq V \leq 0.2 \mu\text{m s}^{-1}$), $S_{\text{hyd}}/S_{\text{img}}$ ranged from 0.1 to 0.3. $S_{\text{hyd}}/S_{\text{img}}$ drastically decreased as V increased, and $S_{\text{hyd}}/S_{\text{img}}$ ranged from 0.004 to 0.02 in the V range of $1.0 \mu\text{m s}^{-1} \leq V \leq 10 \mu\text{m s}^{-1}$. These two velocity ranges correspond to the nodular and disseminated types.

In addition, the boundaries of drastically decreasing $S_{\text{hyd}}/S_{\text{img}}$ shifted to the lower V region as the mixing ratio of 50- μm beads increased, as shown by double-headed arrows in Figure 11. The critical values of V were obtained according to the drastic decrease in $S_{\text{hyd}}/S_{\text{img}}$ corresponding to the boundary of pattern change from massive to nodular and nodular to disseminated, as shown in Figure 10. Thus, it was found that the pattern of hydrate can be classified quantitatively by the boundary obtained by the drastic decrease in $S_{\text{hyd}}/S_{\text{img}}$.

Figure 12 shows the number density of hydrate grains, n_d (N/S_{img}), in units of cm^{-2} , as a function of V for $w_2:w_{50} = 5:5$, 3:7, and 2:8. The regions surrounded by the solid line indicate the region where the massive or nodular type forms. Note that n_d value for the disseminated type is not shown in this figure because the vast majority of the innumerable hydrates in the pore spaces of the glass beads cannot be visualized, with the result that n_d has no meaning. The results indicate that n_d

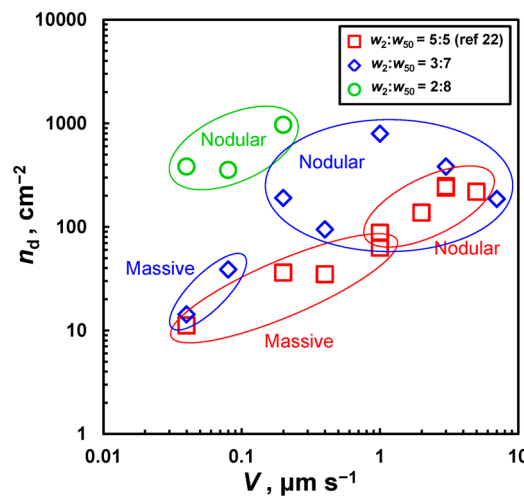


Figure 12. Relationship between the number density of hydrate grains, n_d , and V for $w_2:w_{50} = 5:5$, 3:7, and 2:8. The data points at $w_2:w_{50} = 5:5$ are adopted from the study by Muraoka et al.²²

increased as V increased for all values of $w_2:w_{50}$ over the range of V shown. For $w_2:w_{50} = 5:5$, n_d increased from 10 to 300 cm^{-2} as V increased. For $w_2:w_{50} = 3:7$, n_d increased from 10 to 800 cm^{-2} as V increased. For $w_2:w_{50} = 2:8$, n_d increased from 300 to 1000 cm^{-2} as V increased. In addition, n_d increased as the mixing ratio of 50- μm beads increased in the relatively low-velocity region.

Figure 13 shows the average area of the hydrate grains, S_{hyd}/N , as a function of V at $w_2:w_{50} = 5:5$, 3:7, and 2:8. The regions

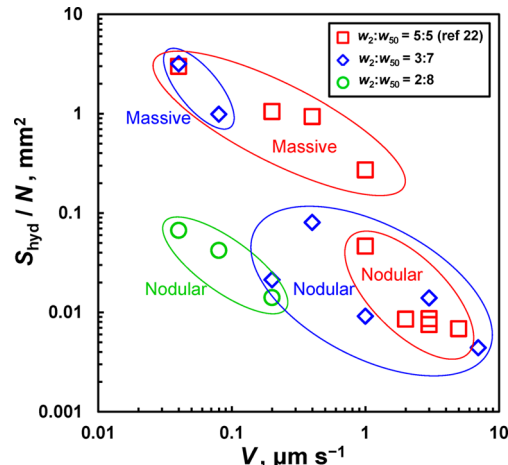


Figure 13. Relationship between the average hydrate area, S_{hyd}/N , and V for $w_2:w_{50} = 5:5$, 3:7, and 2:8. The data points at $w_2:w_{50} = 5:5$ are adopted from the study by Muraoka et al.²²

surrounded by the solid line indicate the region where the massive or nodular type forms. S_{hyd}/N decreased as V increased for all $w_2:w_{50}$. For $w_2:w_{50} = 5:5$, S_{hyd}/N decreased from 3 to 0.007 mm^2 as V increased. For $w_2:w_{50} = 3:7$, S_{hyd}/N decreased from 3 to 0.004 mm^2 . For $w_2:w_{50} = 2:8$, S_{hyd}/N decreased from 0.07 to 0.015 mm^2 . In the lowest V range, S_{hyd}/N is 0.07 mm^2 for $w_2:w_{50} = 2:8$, which is 2 orders of magnitude lower than that of 3 mm^2 for $w_2:w_{50} = 3:7$ or 5:5.

4. DISCUSSION

4.1. Size Scale of Various Hydrate Patterns. In the present study, the various patterns of segregated hydrates such as layered, needle, nodular, and massive were formed as functions of V and $w_2:w_{50}$. First, we discuss the effect of these parameters on the typical size scales of the layered pattern (i.e., X_{hyd} and X_g), as shown in Figure 6. For $w_2:w_{50} = 10:0^{21}$ and $w_2:w_{50} = 8:2$, X_{hyd} and X_g were found to be inversely proportional to V . In addition, both values of X_{hyd} and X_g at $w_2:w_{50} = 8:2$ are larger than those at $w_2:w_{50} = 10:0$. This indicates that increasing the mixing ratio of 50- μm beads resulted in an increase in the size scales of the layered pattern.

Nagashima et al.²¹ showed that X_{hyd} and X_g decreased when the gravimetric solution content, w_s/w_g , of the initial sample decreased. The extrapolated results suggested that X_{hyd} and X_g approached 0 when w_s/w_g decreased to 0.65 (the critical value). This result was applied to the multilayered pattern formation, as schematically illustrated in Figure 14. The gray regions in the image show glass bead-rich regions. The gray scale level indicates the solution content in the glass beads. The bright gray levels indicate high solution content, whereas the dark gray levels indicate low solution content. Figure 14a shows that the solution content is uniform at the initial condition of $w_s/w_g = 1$. The initial layer is represented by the white dot-dashed line. Figure 14b shows that the pure hydrate region formed by displacing glass beads to the right in the figure. Consequently, the region near the growth interface is uniformly consolidated with the glass beads where the solution content decreased. Figure 14c shows that the solution content near the growth interface decreased to the previously mentioned critical value. Subsequently, the hydrate layer stopped forming and transitioned to the pore space type. Figure 14d shows that the hydrate layer formed again in the solution rich region (resulting in a jump of the pure hydrate region). Thus, the multilayered hydrate pattern formed by repeating this process.

Thereby, both the thickness of the hydrate layer, X_{hyd} , and that of the intervals between neighboring layers, X_g , should be affected by the dewatered consolidation region. Takashi et al.²⁶ discussed the dewatering consolidation process for the frost heave of ice in soil. In their study, a consolidation equation obtained by Terzaghi²⁷ was transformed to an equation with a moving frame of reference fixed at the unidirectional freezing front advancing at the freezing velocity, V . It was shown that the length of the dewatered consolidation region, δ_s , was given as $\delta_s = C_v/V$, where C_v is defined as $C_v = k/\gamma_w m_v$. Here, k is the coefficient of the permeability of pore water, γ_w is the unit weight of water, and m_v is the coefficient of the volume compressibility of soil; consequently, δ_s decreases with an increase in V and decrease in k .

The functional form of $\delta_s \propto 1/V$ corresponds to the functional forms of X_{hyd} and X_g vs V , as shown in Figure 6. This indicates that the effect of the length of the dewatered consolidation region, δ_s , is crucial to the size scales of the layered pattern. When the mixing ratio of 50- μm beads increased, X_{hyd} and X_g also increased, as mentioned previously. An increase in the mixing ratio of 50- μm beads increases the permeability of the pore solution, reflected by an increase in the value of k . This is also consistent with the theoretical results indicating that $\delta_s \propto k$. Hence, the size scales of the hydrate layer would be controlled by solution transport to the growing hydrate layer.

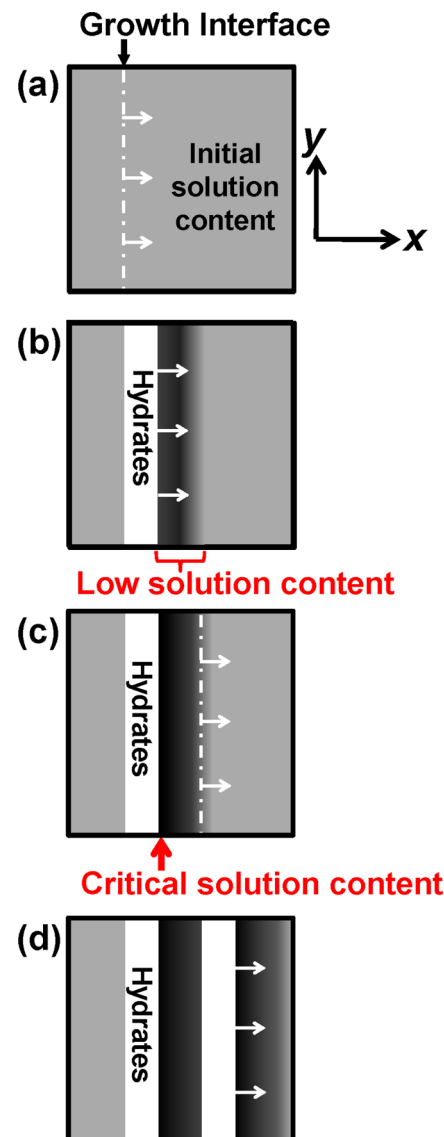


Figure 14. A model for the formation process of the layered hydrate pattern. (a) The initial layer is represented by a white dot-dashed line. The growth interface moves toward the right in the figure. (b) The pure hydrate region formed by displacement of glass beads to the right (white arrows represent the direction) with a moving growth interface. (c) The disseminated type hydrate formed due to the solution content near the growth interface being decreased to the critical value (consolidated by displaced glass beads). (d) The hydrate layer formed again in the solution rich region.

Next, we discuss the effect of V and $w_2:w_{50}$ on the average area of the hydrate grains, S_{hyd}/N , of nodular and massive patterns (Figure 13). As predicted above, S_{hyd}/N is also expected to be larger at lower V because δ_s becomes longer. This corresponds to the experimental results. In short, as V decreased, the average area of hydrate grains, S_{hyd}/N , increased.

Conversely, S_{hyd}/N suddenly decreased when the mixing ratio of 2- μm beads decreased for $w_2:w_{50} = 2:8$. For $w_2:w_{50} = 0:10$ (no 2- μm beads), no visible hydrate grains formed. This trend disagrees with the prediction based on the results of the solution transport theory indicating that $\delta_s \propto k$. This strongly suggests the influence of small beads on the capillary effect. A decrease in the mixing ratio of 2- μm beads diminished the capillary effect, as theoretically shown by Clennell et al.¹⁶ and

the experimental study of Suzuki et al.²⁰ which showed that fine-grained beads promote the displacement of sediment. Thus, to predict the hydrate size scale quantitatively, the results strongly indicate the necessity of a coupled theoretical model taking both the effects of the solution transport and the capillary effect into account.

Next, we discuss the size scale of hydrate patterns at the lowest range of V . Figure 6a,b shows that X_{hyd} and X_g at $V = 0.08 \mu\text{m s}^{-1}$ (i.e., the lowest V applied) for $w_2:w_{50} = 8:2$ deviated substantially below the best fit curve. Using the best fit curve, the sizes are estimated as $X_{\text{hyd}} = 3.4 \text{ mm}$ and $X_g = 4.3 \text{ mm}$ at $V = 0.08 \mu\text{m s}^{-1}$. If the dewatered consolidation region of the THF–water solution reached the edge of the growth cell, solution transport to the growing hydrates would decrease. In addition, since the growth distance to attain steady state is inversely proportional to V ,²⁶ the final stage of the run at the lowest V might be the transition stage before attaining the steady state. The overall directional growth distance was limited by the moving distance (25 mm) of the growth cell.

In addition, the results for $w_2:w_{50} = 5:5$ in the lowest range of $V = 0.2, 0.08$, and $0.04 \mu\text{m s}^{-1}$, given in Figure 5a–c in ref 22, show that the massive hydrate formed in the middle stage of the run and that the hydrate region sizes drastically reduced in the final stage. These results might also reflect the experimental problems associated with the limited length of the growth cell and the limited growth distance in the present experiments. For these reasons, experiments using a longer growth distance in a longer growth cell are required.

4.2. Mechanism of Instability Phenomenon for the Initial Hydrate Layer. In this section, we discuss the mechanism of the instability phenomenon for the growth interface along the y -axis (Figure 3) on the basis of the results of crystal growth experiments (without sediment)²⁸ and a model of the morphological instability of an ice–colloid interface.^{29,30}

Nagashima et al.²⁸ shows the morphological instability of the growth interface of THF hydrate in solution (no glass beads) with the addition of sodium chloride using a directional growth apparatus. The results showed that the growing initially straight interface gradually destabilized into a wedged pattern with time. This phenomenon is called Mullins–Sekerka instability.³¹ Subsequently, some of the wedged hydrates preferentially grew and a larger scale wedged pattern formed. Peppin et al.^{29,30} extended the Mullins–Sekerka instability theory³¹ to address the morphological instability phenomenon of an ice–colloid interface. This theory predicts that the freezing interface in the water (no solutes) can become morphologically unstable owing to the effect of the accumulation of colloidal particles (glass beads) alone. The freezing point depression in the colloidal suspension is given as a function of particle volume fraction. The theory predicts that the freezing point decreases as the particle volume fraction increases when a growing planar ice–clay interface displaces the colloid particles. Hence, the instability phenomenon of an ice–colloid interface can be discussed by incorporating the relation between particle volume fraction and melting temperature in the Mullins–Sekerka instability theory. The theory of Peppin et al. predicts the critical growth rate V , below which the planar clay–ice interface is morphologically stable, and above which the planar clay–ice interface is unstable. Thus, Peppin et al.^{29,30} predicts the critical condition for morphological instability of an ice–colloid interface. Unfortunately, with the lack of physicochemical properties in the present case, and due to the difference of the

initial conditions in the present experiment, a numerical result based on the theory cannot be obtained. Nevertheless, our experimental results show that the power law trends of decreasing wavelength, λ , with increasing V (Figure 3) coincide with the Mullins–Sekerka type instability. Further experimental and theoretical studies are required to quantitatively discuss the present results.

4.3. Formation Mechanism of Various Hydrate Patterns.

In this section, we propose a formation mechanism for the various hydrate patterns by summing up the formation process of the multilayered pattern formed along the x -axis mentioned in section 4.1 and the mechanism of the instability phenomenon of the growth interface along the y -axis given in section 4.2.

Figures 15–17 show schematic illustrations of qualitative formation models for needle, nodular, and massive types. The gray regions in the images show glass bead-rich regions. The bright gray level regions correspond with the high solution content region, and the dark gray level regions correspond with the low solution content region in the glass beads. The white arrows represent the directions of glass bead displacement.

Figure 15 shows the formation process of the needle pattern hydrate. Figure 15a shows that the growth interface becomes wedged shaped due to growth interface instability. Consequently, the glass beads are displaced sideways from the growth tips, as indicated by the white arrows shown in Figure 15b. Figure 15c shows that the convex tips of the growth interface displace the glass beads to both sides of the growth tip. Consequently, the regions near the growth tips are not strongly consolidated with glass beads such that the growth tips can absorb solution constantly. In contrast, the concave bottoms of the growth interface are much more consolidated with the glass beads displaced around the growth tip. Thus, the convex growth tips grow preferentially. This resulted in the formation of the needle pattern, as shown in Figure 15d.

Figure 16 shows the formation process of the nodular pattern hydrate. This formation process might be considered by summing up the multilayer (Figure 14) and needle (Figure 15) pattern formation processes. Figure 16a shows a growth interface shape that is assumed medium shape of the layer and needle formation processes (i.e., the shape of the growth interface is less planar than that shown in Figure 14, and the convex growth tips are less sharper than those shown in Figure 15). Figure 16b shows that the growth tips displace the glass beads toward both sides of the tips. Consequently, the solution contents of regions near the bottoms of the interface diminish to the critical value required to displace the glass beads, as shown in Figure 16c. Simultaneously, the regions near the growth tips are gradually consolidated with glass beads because the convex growth tips are not sharper than that of the needle pattern. Consequently, the solution content near the growth tips finally reaches the critical condition to displace glass beads. Figure 16d shows that the formation of pure hydrate regions stops and that the disseminated type forms in front of the growth tips. Subsequently, the pure hydrate regions form again in the solution rich region. Thus, the nodular pattern is formed by repeating this process.

Figure 17 illustrates the pattern change from nodular to massive. The massive pattern formed in the lowest growth rate region for intermediate to higher ratios of 50- μm beads (Figure 10). When the growth rate is low and the coefficient of permeability of pore water is large, the length of the consolidation region, δ_s , becomes long. Each nodular hydrate

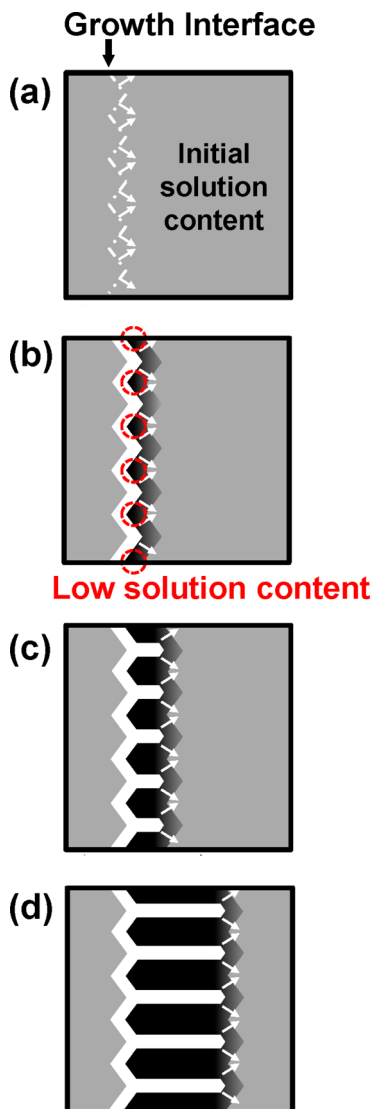


Figure 15. A model for the formation process of the needle hydrate pattern. (a) The growth interface becomes wedge shaped due to growth interface instability. (b) The glass beads are displaced at an acute angle relative to the growth direction. (c) The region near the growth tips is not strongly consolidated with the glass beads, and the growth tips can absorb solution constantly. (d) The needle pattern hydrate forms due to the preferential growth of the convex growth tips.

can absorb more solution from the larger area. Consequently, some nodular hydrates grow to an extremely large size along the x - and y -axes; thus, the residual glass bead-rich regions are quite small compared with the extremely large nodular hydrates. An aggregate consisting of this extremely large pure hydrate region and the quite small glass bead-rich region can be identified as the massive type according to the definition by Malone.³

We first proposed the qualitative models for the formation processes of needle, nodular, and massive patterns based on the frost heave theory.^{16,26,29,30} Note that the validation of the present model must be performed by further experimental studies and improved theories (i.e., time dependent theoretical studies that consider solution transport and capillary effect, which are able to predict the morphological instability and jumps of pure hydrate regions involved with types such as

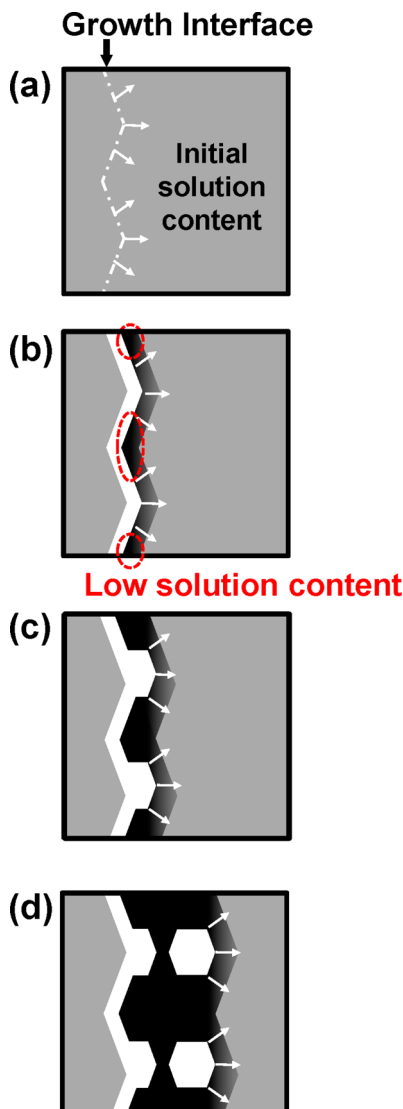


Figure 16. A model for the formation process of the nodular hydrate pattern. (a) The shape of the growth interface is assumed medium shape of the layer and needle formation processes. (b) The growth tips displace the glass beads toward both sides of the tips. (c) The solution content of the regions near the bottoms of the interface becomes lower than the critical value required for displacement of the glass beads. Simultaneously, the regions in front of the growth tips are gradually consolidated with glass beads. (d) The formation of pure hydrate regions stops, and the disseminated type forms in front of the growth tips. Then, the pure hydrate regions form again in the solution rich region.

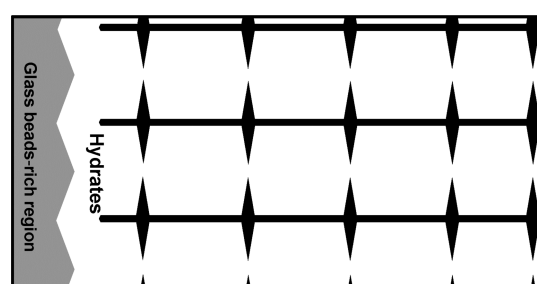


Figure 17. A model for the pattern change from the nodular to the massive pattern.

multilayer and nodular). To discuss jumps of pure hydrate regions, it is important to clarify the critical solution content. Nagashima et al.²¹ estimated the critical solution content for $w_2:w_{50} = 10:0$ (layered pattern condition) by extrapolating experiment results. The values of critical solution contents for $w_2:w_{50} = 8:2$, 5:5, and 3:7 (i.e., layer, nodular, and needle pattern formation conditions) must be obtained by further study depending on the initial solution content or by direct measurement of the solution content distribution in the experiment cell.

For applying the results of the present study to marine hydrate formation, it is also noted that the sediment in hydrate-stable regions beneath the ocean is subjected to effective overburden pressure by overlying sediments. The experiments in the present study were conducted without confined stress for simplicity. Thus, experimental studies for the measurement of phase pressure of hydrates formed in sediment and the growth pattern dependence of confined pressure are required.

In marine settings, most gas hydrates probably form from an aqueous phase.¹³ This diffusion-limited process is too slow to form methane hydrate patterns by laboratory experiments.¹⁴ This suggests that the time scale of hydrate pattern formation in sediments in nature might be considerably longer than the duration time of an experimental run. Therefore, as a first step, our group performed studies using a stoichiometric THF–water solution to clarify only the effect of the sediment by eliminating the diffusion-limited effect of guest molecules from the model system. However, to clarify the formation mechanism of methane hydrate in oceanic sediment, the effect of the sediment and the diffusion-limited process of guest molecules must be considered. The growth rate might be lowered due to the diffusion-limited process of guest molecules dissolved in water. This might also affect the pattern and size scales of hydrate in the soil model. Formation experiments of THF hydrates in glass bead containing a dilute THF–water solution are underway as a second step. The results will be reported in a separate paper.

5. CONCLUSIONS

We observed the pattern formation of THF clathrate hydrates in a mixture composed of a THF–17H₂O solution and glass beads of two sizes (2 and 50 μm diameter) as functions of growth rate and glass bead mixing ratios (by weight). The overall growth rate, V , of the hydrates was controlled using a directional growth apparatus.

The results showed that the growth interface of the initial hydrate layer destabilized with growth. The wavelength, λ , of the destabilized initial hydrate layer decreased according to a power law as the growth rate, V , increased. After the initial hydrate layer formed, various patterned hydrates formed depending on the mixing ratio of the glass beads, $w_2:w_{50}$, and the growth rate, V . The results showed that a multilayered pattern formed in the mixture for $w_2:w_{50} = 8:2$. For $w_2:w_{50} = 10:0$ ²¹ and $w_2:w_{50} = 8:2$, X_{hyd} (the average thickness of the hydrate layer) and X_g (the average thickness of the interval between neighboring hydrate layers) were determined to be inversely proportional to V . In addition, both values of X_{hyd} and X_g at $w_2:w_{50} = 8:2$ were larger than those at $w_2:w_{50} = 10:0$. We are the first to successfully obtain a needle pattern, which was found to form at $w_2:w_{50} = 3:7$ and $V = 7.0\text{--}8.0 \mu\text{m s}^{-1}$. The formed hydrate patterns were classified into a diagram in accordance with the growth rate, V , and the mixing ratio of glass beads, $w_{50}/(w_2 + w_{50})$. The obtained images of the various

hydrate patterns were analyzed. The boundaries between disseminated and nodular, and nodular and massive patterns were determined not only by visual appearance but also by the quantitative method proposed by Muraoka et al.²² The hydrate image analysis results showed that the segregated growth area of the hydrates, $S_{\text{hyd}}/S_{\text{img}}$, and the average hydrate area, S_{hyd}/N , increased, and the number density of hydrate grains, n_d (N/S_{img}), decreased with decreasing V .

The size scale of various hydrate patterns was discussed using the frost heave model. The functional form of the dewatered consolidation region, $\delta_s \propto V$, derived theoretically by Takashi et al.²⁶ corresponded to the functional forms of X_{hyd} and X_g vs V determined for the multilayered type hydrate. Moreover, it was shown that the length of the dewatered consolidation region, δ_s , was proportional to the permeability of the pore solution, k .²⁶ The values of X_{hyd} and X_g also increased when the mixing ratio of the 50-μm beads increased. The increase in the mixing ratio of 50-μm beads increases the permeability of the pore solution, k , which is also consistent with the theoretical results of $\delta_s \propto k$. The average areas of the hydrate grains, S_{hyd}/N , of the nodular and massive patterns are also expected to be larger at lower V since δ_s becomes longer, which corresponds with our experimental results. Hence, as V decreased, the average area of hydrate grains, S_{hyd}/N , increased. Conversely, S_{hyd}/N suddenly decreased when the mixing ratio of 2-μm beads decreased at $w_2:w_{50} = 2:8$. This trend disagrees with the prediction based on the results of the solution transport theory reflected by the relation $\delta_s \propto k$. This strongly suggests the influence of small beads on the capillary effect. The decrease in the mixing ratio of 2-μm beads resulted in a diminished capillary effect, as theoretically shown by Clennell et al.¹⁶ and the experimental study by Suzuki et al.,²⁰ which showed that fine-grained beads promoted displacement of sediment.

We discussed the mechanism of the instability phenomenon of the growth interface along the y -axis. The power law trends of the wavelengths, λ , decreased as V increased, quantitatively coinciding with the morphological instability model of an ice–colloid interface by Peppin et al.^{29,30} based on the Mullins–Sekerka instability theory.³¹

We first proposed the qualitative models for the formation processes of needle, nodular, and massive patterns by summing up the formation process of the multilayered pattern formed along the x -axis and the mechanism of the instability phenomenon of the growth interface along the y -axis in accordance with the frost heave theory.^{16,26,29,30} The formation process of the multilayered pattern (discontinuous pattern along the x -axis) was qualitatively explained by the frost heave theory,²¹ and the needle pattern (the discontinuous pattern along the y -axis) was qualitatively explained by the morphological instability model (Peppin et al.^{29,30}). In addition, we showed that the formation processes of the nodular and massive patterns (the discontinuous pattern along the x -axis and y -axis) could be explained by summing up the multilayer and needle pattern formation processes.

We successfully reproduced various hydrate patterns and classified them into a hydrate pattern diagram (the dependence of the hydrate growth pattern on V and $w_2:w_{50}$), and the results were qualitatively consistent with the theoretical model for frost heave and the morphological instability model. In addition, we proposed pattern formation models for needle, nodular, and massive pattern hydrates in porous sediment.

AUTHOR INFORMATION

Corresponding Author

*E-mail: knaga@isc.meiji.ac.jp. Phone/Fax: +81-44-934-7269.
Web: <http://www.isc.meiji.ac.jp/~icephys/IPG-eng.html>.

Present Address

[#]National Institute of Advanced Industrial Science and Technology, 16-1 Onogawa, Tsukuba-shi, Ibaraki, 305-8569, Japan.

Notes

The authors declare no competing financial interest.

ACKNOWLEDGMENTS

This work was partly supported by JSPS KAKENHI Grant Number 21540498.

REFERENCES

- (1) Sloan, E. D., Jr.; Koh, C. A. In *Clathrate Hydrates of Natural Gases*, 3rd ed.; CRC Press: Boca Raton, FL, 2008; Chapter 7, p 561.
- (2) Kvenvolden, K. A. *Terra Nova* **2002**, *14*, 302–306.
- (3) Malone, R. D. *Gas Hydrate Topical Report*; DOE/METC/SP-218; U.S. Department of Energy: Washington, DC, April 1985.
- (4) Paull, C. K.; Ussler, W.; Borowski, W. S. *N.Y. Acad. Sci.* **1994**, *715*, 392–409.
- (5) Tohidi, B.; Anderson, R.; Clennell, M. B.; Burgass, R. W.; Biderkab, A. B. *Geology* **2001**, *29*, 867–870.
- (6) Katsuki, D.; Ohmura, R.; Ebinuma, T.; Narita, H. *Philos. Mag.* **2006**, *86*, 1753–1761.
- (7) Katsuki, D.; Ohmura, R.; Ebinuma, T.; Narita, H. *Philos. Mag.* **2007**, *87*, 1057–1069.
- (8) Taber, S. J. *Geol. (Chicago, IL, U.S.)* **1929**, *37*, 428–461.
- (9) Taber, S. J. *Geol. (Chicago, IL, U.S.)* **1930**, *38*, 303–317.
- (10) Watanabe, K. *J. Cryst. Growth* **2002**, *237*–*239*, 2194–2198.
- (11) Hiroi, M.; Mizusaki, T.; Tsuneto, T.; Hirai, A.; Eguchi, K. *Phys. Rev. B: Condens. Matter Mater. Phys.* **1989**, *40*, 6581–6590.
- (12) Zhu, D.-M.; Vilches, O. E.; Dash, J. G.; Sing, B.; Wettlaufer, J. S. *Phys. Rev. Lett.* **2000**, *85*, 4908–4911.
- (13) Buffett, B. A.; Zatsepina, O. Y. *Mar. Geol.* **2000**, *164*, 69–77.
- (14) Rempel, A. W.; Buffett, B. A. *J. Geophys. Res.: Solid Earth* **1997**, *102*, 10151–10164.
- (15) Krause, F. F. *Sediment. Geol.* **2001**, *145*, 189–213.
- (16) Clennell, M. B.; Hovland, M.; Booth, J. S.; Henry, P.; Winters, W. J. *J. Geophys. Res.: Solid Earth* **1999**, *104*, 22985–23003.
- (17) Scherer, George, W. *J. Non-Cryst. Solid* **1993**, *155*, 1–25.
- (18) Jeffrey, G. A. In *Inclusion Compounds*; Atwood, J. L., Davies, J. E. D., MacNicol, D. D., Eds.; Academic Press: New York, 1984; Vol. 1, p 135.
- (19) Gough, S. R.; Davidson, D. W. *Can. J. Chem.* **1971**, *49*, 2691–2699.
- (20) Suzuki, T.; Muraoka, M.; Nagashima, K. *J. Cryst. Growth* **2011**, *318*, 131–134.
- (21) Nagashima, K.; Suzuki, T.; Nagamoto, M.; Shimizu, T. *J. Phys. Chem. B* **2008**, *112*, 9876–9882.
- (22) Muraoka, M.; Nagashima, K. *J. Phys. Chem. C* **2012**, *116*, 23342–23350.
- (23) Nagashima, K.; Furukawa, Y. *J. Cryst. Growth* **1997**, *171*, 577–585.
- (24) Nagashima, K.; Furukawa, Y. *J. Phys. Chem. B* **1997**, *101*, 6174–6176.
- (25) Pötschke, J.; Rogge, V. *J. Cryst. Growth* **1989**, *94*, 726–738.
- (26) Takashi, T.; Ohrai, T.; Yamamoto, H. *Jpn. Soc. Snow Ice* **1977**, *39*, 53–64, <http://dx.doi.org/10.5331/seppyo.39.53>.
- (27) Terzaghi, K. *Erdbaumechanik auf Bodenphysikalischer Grundlage*; Franz Deuticke: Vienna, 1925.
- (28) Nagashima, K.; Yamamoto, Y.; Takahashi, M.; Komai, T. *Fluid Phase Equilib.* **2003**, *214*, 11–24.
- (29) Peppin, S. S. L.; Wettlaufer, J. S.; Worster, M. G. *Phys. Rev. Lett.* **2008**, *100*, 238301.
- (30) Peppin, S. S. L.; Majumdar, A.; Wettlaufer, J. S. *Proc. R. Soc. London, Ser. A* **2010**, *466*, 177–194.
- (31) Mullins, W. W.; Sekerka, R. F. *J. Appl. Phys.* **1964**, *35*, 444.